ACS APPLIED MATERIALS & INTERFACES

Research Article

www.acsami.org

Nitrogen/Carbon Atomic Ratio-Dependent Performances of Nitrogen-Doped Carbon-Coated Metal Oxide Nanocrystals for Anodes in Lithium-Ion Batteries

Yemeng Ni,[†] Yajing Yin,[†,‡] Ping Wu,*[,†] Hui Zhang,[†] and Chenxin Cai*[,†]

[†]Jiangsu Key Laboratory of New Power Batteries, Jiangsu Collaborative Innovation Center of Biomedical Functional Materials, College of Chemistry and Materials Science, Nanjing Normal University, Nanjing 210097, P. R. China

[‡]Jiangsu Second Normal University, Nanjing 210013, P. R. China

Supporting Information

ABSTRACT: We report the hydrothermal synthesis of the N-doped carbon-coated NiO nanocrystals (N−C−NiO NCs) with tunable N/C atomic ratios using the nitrogen-containing ionic liquids (ILs) as new carbon precursor, and the N-doped carbon layer composition-dependent performances of N−C−NiO NCs anode for lithium-ion batteries (LIBs). The results indicate that the N-doped carbon coating can significantly enhance the electronic conductivity, effectively avoid the problems of cracking or pulverization of the NiO, and prevent the aggregation of the active materials upon cycling. These properties make the synthesized material a promising anode material for LIBs. The N−C−NiO NCs with the N/C atomic ratio of 21.2% in the N-doped carbon layer show a high specific capacity of ~710 mAh g^{-1} at a current rate of 0.3 C (very closed to the theoretical capacity of 718 mAh g^{-1} for NiO), a high rate capability (still able to deliver a discharge capacity of ~430 mAh g^{-1} at a current density of 10 C), and good capacity retention upon cycling (maintains at 710 mAh g^{-1} at least up to the 50th cycle) compared with those of pristine NiO nanoparticles. Moreover, the electrochemical performances of the N−C−NiO NCs depend on the composition (N/C atomic ratios) in the N-doped carbon layer and are enhanced with increasing of the N/C ratios. Our approach offers an effective and convenient technique to improve the specific capacities and rate capabilities of highly insulating electrode materials for batteries and may also provide general and effective approach toward the synthesis of other metal oxides coated with N-doped carbon layer.

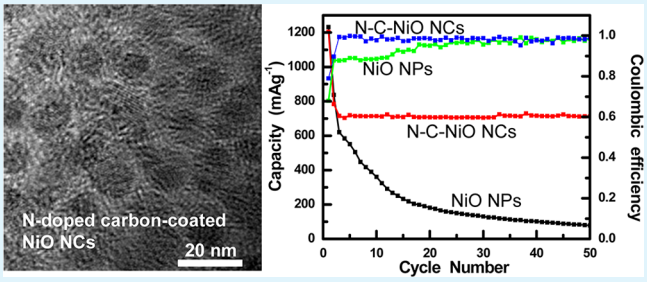

KEYWORDS: *lithium-ion batteries, anode material, metal oxide, nickel oxide nanocrystals, nitrogen-doped carbon, ionic liquids*

1. INTRODUCTION

With the increasing environmental problem caused by the extensive utilization of conventional energy sources and the gradual depletion of oil and coal resources around the world, the development of clean and highly efficient energy storage system is becoming an even more urgent need. As an electrochemical energy storage device, lithium-ion batteries (LIBs), which show the highest energy density of rechargeable batteries, have attracted significant attention within the past few decades and have exhibited a wide range of applications ranging from consumer devices and portable electronics to electric vehicles, hybrid electric vehicles, and large-scale stationary energy storage.[1−15] However, the performance of current LIBs cannot meet the requirements in these areas in terms of high power density, long cycle life, and safety.

Because the charge−discharge of LIBs is achieved through the intercalation−extraction process of lithium ions in the electrodes, the nature of electrode materials acting is crucial to the performance of the battery. Graphite has been widely used as the anode material in commercial LIBs due to its natural abundance and stable cycling performance. However, its theoretical specific capacity is relatively low (e.g., ~372 mAh g^{-1}, based on the formation of LiC_6)[16] and cannot meet the requirements of the next-generation LIBs. To enhance the battery performance, alternative electrode materials are required. Recently, transition metal oxides have been widely investigated as anode materials for LIBs and have attracted great interest because of their low cost, high theoretical capacities (500−1000 mAh g^{-1}), environmentally friendly synthesis processes, and structural stability and diversity.[2,17−31] However, metal oxide-based anode materials always suffer from rapid capacity fading and unsatisfactory rate performance caused by the poor conductivity and the severe pulverization occurring in the cycling process.[32−35] The pulverization problem is mainly due to the large volume changes and consequent local strain generated during the lithium ion intercalation-extraction process. This pulverization simultaneously leads to the interruption of the ionic and

Received: February 5, 2014
Accepted: April 14, 2014
Published: April 14, 2014

electronic conduction pathways in the electrode. The most effective way to improve capacity retention and the rate performances is coating/hybridizing the metal oxide with a thin layer of conductive material (such as carbon)[26,27,31,36−39] or the preparation of a small and homogeneous particle size distribution with a designed morphology (such as hollow structures, porous structures etc.).[24,28,40,41] The reduction of particle size (for example nanometer scale particles) can partially suppress the expansion and shrinkage of the electrode materials, shorten the diffusion pathways for both electrons and lithium ions, and increase the electrode−electrolyte contact area, so that the electroactivity and the rate capacity of the electrode can be improved. The coating/hybridizing metal oxide with conducting carbon, for example, amorphous carbon shell, carbon nanotubes (CNTs), or graphene sheets can improve the surface electronic conductivity and the electric contact between electrode materials and conducting agents, and, in turn, leads to an improvement of LIBs. Conventional surface carbon-coating approach includes pyrolysis of sugar,[42] and polymer[43,44] etc. However, these methods need high temperature treatment or involve complex processes and/or equipment. Moreover, most of the previous efforts have been paid to tune the crystallinity, thickness and uniformity of the carbon-coating. There are few reports on tuning the composition of the carbon-coating and studying the carbon-coating composition-dependent performances of electrode materials to optimize the electrochemical performance of LIBs.

This work reports the synthesis of the nitrogen-doped (N-doped) carbon-coated nickel oxide nanocrystals (denoted as N−C−NiO NCs) with the tunable N/C atomic ratios using the nitrogen-containing ionic liquids (ILs) as new carbon precursor, and the N-doped carbon layer composition-dependent performances of N−C−NiO NCs anode in LIBs. We used NiO as a model system because it is one of the most promising anode materials with high safety, environmental benignity, low cost, and outstanding theoretical capacity of 718 mAh g^{-1}.[36,45] The use of N-containing ILs as carbon precursors has several advantages.[46−50] Compared with conventional solid carbon precursors, ILs can coat the surface of the materials easily because of their fluidic properties. The pyrolysis of ILs with very low vapor pressure can occur in the wide temperature range of 400−1000 °C without drastic solvent evaporation.[49,50] This is favorable for forming a thin uniform coating layer on material surface. In addition, the composition of the coating layer can easily be tuned by selecting ILs containing different N/C atomic ratios. More importantly, the properties of the interphase formed between the active substrate and the coating layer, which is essential for material design and optimization, can also be easily tuned.[48] We first synthesized and characterized N−C−NiO NCs, and then studied their improved performances as anode in LIBs. Finally, we compared the performances of the N−C−NiO NCs anode material at different N/C atomic ratios in the N-doped carbon coating and highlighted the carbon coating composition-dependent performances of the N−C−NiO NCs. We believe this work opens a new and exciting possibility for enhancing the performance of anode of LIBs, and our method can provide a highly effective approach that can be readily scaled up for real application.

2. EXPERIMENTAL SECTION

2.1. Synthesis of N−C−NiO NCs. The chemicals we used were analytical grade and purchased from Shanghai Chemical Reagent Co. Ltd. (Shanghai, China). $EMImBF_4$ (99%), $BMImBF_4$ (99%), and $HMImBF_4$ (99%) were from Sigma-Aldrich and used as received.

The $Ni(HCO_3)_2$ precursors were prepared from Ni^{2+} ions in ethylene glycol (EG) by solvothermal method. $NiCl_2{\cdot}6H_2O$ (~0.9 g) was dissolved into 20 mL of EG containing 1.2 g of CH_3COONa and 1.2 g of urea.[51] The solution was stirred under 250 rpm for 5 h at an ambient temperature. After complete dissolution, the solution was transferred into a Teflon-lined autoclave (40 mL) with autoclave capacity of less than 80%. After it was sealed, the autoclave was heated to 180 °C and maintained at this temperature for 22 h, and then allowed to naturally cool to an ambient temperature. $Ni(HCO_3)_2$ precursors were collected by centrifugation at 10 000 rpm for 15 min, washed with ethanol and deionized water for at least three times, and dried overnight at 80 °C.

For synthesizing the N−C−NiO NCs, we ultrasonically dispersed the $Ni(HCO_3)_2$ precursors (0.03 g) into 5 mL of $EMImBF_4$ for ~10 min. Then, the mixture was transferred into a Teflon-lined autoclave (20 mL). The autoclave was heated to 180 °C and maintained at the temperature for 4 h. After the autoclave was cooled naturally to an ambient temperature, the $EMImBF_4$-coated $Ni(HCO_3)_2$ nanostructures were collected by centrifugation at 10000 rpm, washed with ethanol and deionized water for three times, and dried overnight at 60 °C under vacuum. The N−C−NiO NCs were obtained by calcination of the $EMImBF_4$-coated $Ni(HCO_3)_2$ nanostructures at 350 °C under Ar atmosphere for 3 h and then at ~280 °C in air for 2 h.

With the use of similar procedures, the BM−N−C−NiO NCs and HM−N−C−NiO NCs were also synthesized by replacing the $EMImBF_4$ with $BMImBF_4$ and $HMImBF_4$, respectively. The pristine NiO nanoparticles (NiO NPs, without coating with carbon layer) were prepared by calcining the $Ni(HCO_3)_2$ precursor (without coating with ILs) using the similar procedures as depicted above.

2.2. Instruments. Scanning electron microscopic (SEM) images were recorded using a JSM-7600F field-emitting scanning electron microscope. The transmission electron microscopic (TEM) and high-resolution TEM (HRTEM) images were carried out on a JEM−2100F transmission electron microscope. X−ray diffraction (XRD) patterns were measured using Rigaku/Max-3A X-ray diffractometer with Cu Kα radiation (λ = 0.15418 nm). X-ray photoelectron spectroscopy (XPS) was recorded on an ESCALAB 250 XPS spectrometer (VG Scientifics) using the monochromatic Al Kα line at 1486.6 eV. The binding energies were calibrated with respect to the C (1s) peak at 284.6 eV. The peak was analyzed based on curve-fitting with a mixed Gaussian−Lorentzian line shape using the XPS PEAK program (version 4.0). The thermogravimetric analysis (TGA) was carried out on a PerkinElmer Diamond instrument in air at a ramping rate of 2 °C min^{-1}.

2.3. Electrochemical Measurements. The electrochemical performance of the N−C−NiO NCs as an anode for LIBs was evaluated in coin-type half cells (2025-type) at an ambient temperature. The half cells were assembled in the high-purity argon-filled glovebox (IL-2GB, Innovative Technology) with the synthesized N−C−NiO NCs as the working electrode materials. The working electrodes were prepared by dispersing the synthesized products (80 wt %), acetylene carbon black (Super-P, 10 wt %), and poly(vinylidene fluoride) binder (PVDF, 10 wt %) in *N*-methyl-2-pyrrolidone (NMP) solvent to form a slurry. The slurry was then pasted onto a Cu foam current collector and was dried at 120 °C for 12 h under vacuum. Thin Li foil was employed as the counter electrode, and a polypropylene membrane (Celgard 2400) was used the separator. The electrolyte solution was 1 M $LiPF_6$ dissolved in a mixture of ethylene carbonate (EC) and dimethyl carbonate (DMC) with a volume ratio of 1:1. Cyclic voltammograms (CVs) and electrochemical impedance spectroscopy (EIS) were measured on a using an Autolab PGSTAT302N electrochemical station (Metrohm) at ambient temperature. CVs were recorded in the potential range of 0−3.0 V (vs Li^+/Li redox couple) at a potential scan rate of 0.1 mV s^{-1}, and EIS was measured over the frequency range from 100 kHz to 0.01 Hz. The galvanostatic charge−discharge measurements were conducted on LAND battery test system (CT2001A) at different current densities between cutoff potentials of 0−3 V (vs Li^+/Li redox couple). The discharge and

charge capacities were calculated based on the total mass of NiO NCs and N-doped carbon layer in the materials.

3. RESULTS AND DISCUSSION

3.1. Synthesis of the N−C−NiO NCs. To synthesize the N−C−NiO NCs, we first prepared the $Ni(HCO_3)_2$ precursors from Ni^{2+} ions in urea-contained ethylene glycol (EG) solution by solvothermal method at 180 °C. The formation process of $Ni(HCO_3)_2$ precursors can be depicted as follows:[51]

$$CO(NH_2)_2 + 3H_2O \rightarrow 2NH_3{\cdot}H_2O + CO_2 \quad (1)$$

$$NH_3{\cdot}H_2O \rightarrow NH_4^+ + OH^- \quad (2)$$

$$CO_2 + 2OH^- \rightarrow CO_3^{2-} + H_2O \quad (3)$$

$$CO_3^{2-} + H_2O + CO_2 \rightarrow 2HCO_3^- \quad (4)$$

$$Ni^{2+} + 2HCO_3^- \rightarrow Ni(HCO_3)_2 \quad (5)$$

When the urea-contained EG solution is heated to 180 °C, urea undergoes hydrolysis and releases CO_2 and OH^- ions through reactions 1 and 2. The generated CO_2 will be transformed into CO_3^{2-} ions according to reaction 3. When the concentration of urea is high (1 M in this work), the large amount of CO_2 produced from reaction 1 would further react with CO_3^{2-} ions to form HCO_3^- ions, which then react with Ni^{2+} to generate $Ni(HCO_3)_2$ precursor (reaction 5). As the reaction proceeds, the concentration of $Ni(HCO_3)_2$ in the solution will reach saturation, forming $Ni(HCO_3)_2$ crystal nuclei and subsequently growing into nanostructures (please refer to Figure S1 for the detailed characterization of the prepared $Ni(HCO_3)_2$ precursors).

After the precursors were coated with $EMImBF_4$ (1-ethyl-3-methylimidazolium tetrafluoroborate) at 180 °C for 4 h, they were calcined at 350 °C under Ar atmosphere for 3 h and then at ∼280 °C in air for 2 h to obtain the EM−N−C−NiO NCs (to distinguish the N−C−NiO NCs prepared using different ILs, we denoted them as EM−N−C−NiO NCs, BM−N−C−NiO NCs, and HM−N−C−NiO NCs for the N−C−NiO NCs prepared using $EMImBF_4$, $BMImBF_4$ (1-butyl-3-methylimidazolium tetrafluoroborate), and $HMImBF_4$ (1-hexyl-3-methylimidazolium tetrafluoroborate), respectively). XRD patterns of the EM−N−C−NiO NCs depicted in Figure 1A (curve a) show that all of the diffraction peaks are the same as those for pristine NiO nanoparticles (curve b. For comparison, we prepared NiO nanoparticles (NiO NPs) with the size of ∼20 nm (Figure S2) by calcining the $Ni(HCO_3)_2$ precursor (without coating with ILs) using the similar procedures as those for EM−N−C−NiO NCs). These characteristic peaks ((111), (200), (220), (311), and (222)) can be indexed to cubic NiO (JCPDS No. 071-1179). The diffraction peaks are sharp, implying high crystalline of the NiO NCs. However, the (002) diffraction peak of carbonaceous materials typically located at ∼25°[49] is not observed in patterns of EM−N−C−NiO NCs (curve a, Figure 1A). This is probably due to the low content of carbon layer in the synthetic materials (∼10.7% in weight, please refer to the discussion presented below) and the diffraction of carbon layer is quite weaker as compared to the well-crystalline NiO NCs. To confirm the presence of N-doped carbon layer, Raman spectra of the EM−N−C−NiO NCs were recorded. We found the characteristic Raman peaks of NiO (∼482 cm^{-1}. The Raman spectrum of pristine NiO NPs is depicted in curve b in Figure 1B) and characteristic peaks of

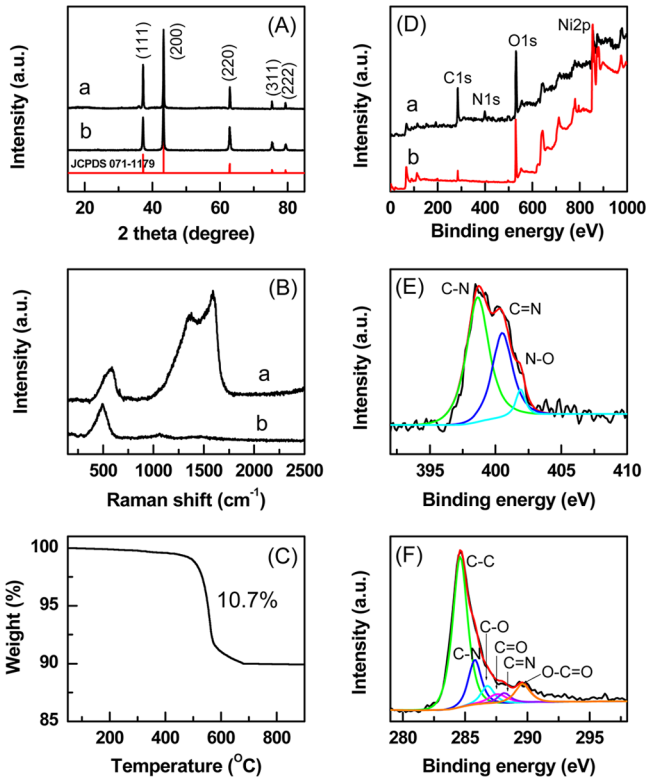

Figure 1. XRD patterns (A), Raman (B), TGA curve (C), and XPS survey spectra (D) of the EM−N−C−NiO NCs (curve a) and pristine NiO NPs (curve b). (E and F) High-resolution XPS spectra of N 1s (E) and C 1s (F), and their related curve-fitted components. The black line represents the measured data, and the red line represents the curve-fitted data.

carbonaceous materials at ∼1592 cm^{-1} (G-band, originating from the in-plane stretch vibration of carbon atoms) and 1356 cm^{-1} (D-band, originating from the breathing-vibration of carbon atoms) (curve a, Figure 1B), confirming the existence of carbon in the prepared materials. The content of N-doped carbon was determined by TGA measurements, which show the product consisting ∼10.7% N-doped carbon and ∼89.3% NiO in weight (Figure 1C).

We used XPS to characterize the detailed information about the elemental compositions of N-doped carbon layer. The survey scan spectrum for EM−N−C−NiO NCs shows C 1s (at ∼284.6 eV), N 1s (at ∼399.0 eV), O 1s (at ∼531.9 eV), and Ni 2p peaks (at ∼855.1 eV) with the N/C atomic ratio of ∼21.2%, which is estimated from N 1s and C 1s peaks (curve a in Figure 1D). However, XPS survey spectra of pristine NiO NPs only shows the presence of C 1s, O 1s, and Ni 2p peaks, the N 1s signal is too low to be certainly detected (curve b in Figure 1D). These results suggest the presence of N in the coating layer. Deconvoluting N 1s peak can provide more detailed information on nitrogen functional groups. It is widely established that incorporation of nitrogen atoms into carbon materials can result to the formation of different kinds of nitrogen functionalities such as pyrrolic, pyridinic, and nitrile groups[52,53] etc. The nitrogen atom can also substitute for a carbon atom forming substitutional or graphitic nitrogen. The existence of these functionalities depends on the experimental conditions. For the EM−N−C−NiO NCs, the N peak can be deconvoluted into three peaks (Figure 1E): the peaks at binding energies of 398.6, 400.6, and 402.0 eV, which can be

ascribed to C−N, C═N, and N−O bonds,[53] respectively. The nitrogen atomic compositions of C−N, C═N, and N−O are ∼57.4%, 35.4%, and 7.2%, respectively (note that we cannot exclude the possibility of the existence of the C ≡ N bond, because its binding energy is very close to that of the C−N bond). These results indicates different configurations of nitrogen in N-doped carbon layer: pyridine-like nitrogen with a C−N bond together with a C═N bond, graphite-like nitrogen with three C−N bonds, and oxidized nitrogen with two C−N bonds and a N−O bond.

The carbon functionalities and their distribution in the N-doped carbon layer are also identified by deconvoluting the C 1s peak into its relative components (Figure 1F). Two main peaks at ∼284.6 and 286.8 eV are ascribed to C−C and C−O (includes epoxide and hydroxyl) bonds, respectively. The peaks at ∼287.7 and 289.6 eV are assigned to C═O and O−C═O, respectively. In addition, the C−N peak (∼285.8 eV),[54] and C═N (∼288.2 eV)[55] can be certainly identified, further demonstrating the formation of the N-doped carbon layer on the surface of NiO NCs.

The morphologies and structures of the EM−N−C−NiO NCs were observed from TEM and SEM. High-magnification TEM image shows a nearly uniform size distribution of NiO NCs with an average size of ∼10−15 nm (Figure 2A). The NiO

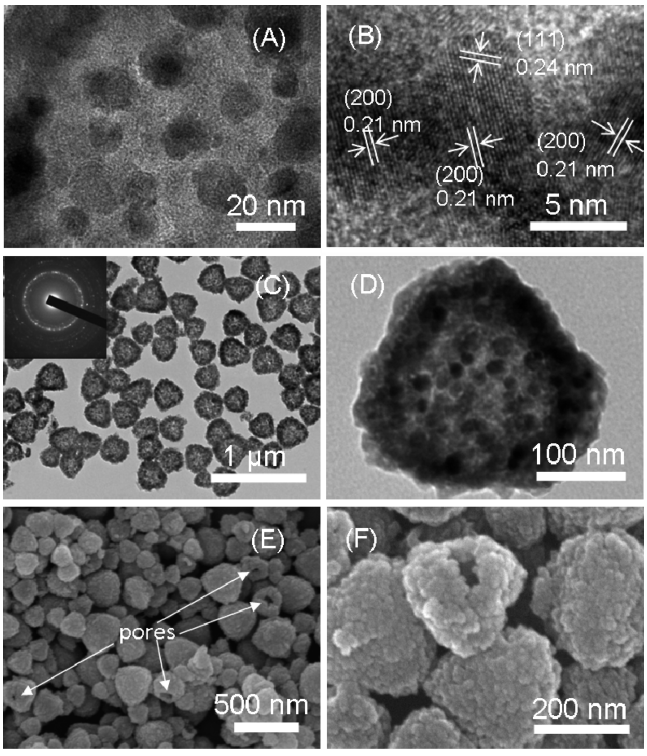

Figure 2. TEM (A, C, and D), HRTEM (B), and SEM images (E and F) of the prepared EM−N−C−NiO NCs. The inset in (C) shows the SAED pattern of NiO NCs. The EM−N−C−NiO NCs are assembled to form hollow structured cluster networks with sizes of ∼250−300 nm.

NCs are coated with a layer of N-doped carbon. The high-resolution TEM (HRTEM) image of single NiO NC (Figure 2B) identifies the lattice spacing of 0.24 and 0.21 nm, which correspond to the interspaces of the (111) and (200),[36] respectively, planes of NiO. HRTEM image also indicates the amorphous nature of the N-doped carbon layer (Figure 2B). The elected area electron diffraction (SAED) pattern (inset in Figure 2C) shows concentric rings composed of bright discrete diffraction spots, indicating that the NiO NCs have a high degree of crystallinity. These NiO NCs are typically assembled to form cluster networks with sizes of ∼250−300 nm (Figure 2C). The formed clusters have a hollow structure (Figure 2C, D), which is clearly revealed by the contrast between the shells and hollow interiors (Figure 2D). The thickness of the shell is about 20 nm. The hollow nature of the clusters can also be demonstrated by some broken clusters, as observed in SEM image (Figure 2E). Another feature of the formed clusters is that their surfaces are rough and consist of many nanoparticles with a size of ∼10 nm as revealed by the high-magnification SEM image (Figure 2F). These characteristics make the EM−N−C−NiO NCs be good anode materials in LIBs because the small size of the NiO NCs can reduce the traveling path for electrons and Li^+ ions, facilitating Li^+ ion exchange across the interfaces. The N-doped carbon coating and the assembled hollow structures of the cluster can tolerate the large volume change in the electrodes during the course of extraction and insertion of Li^+ ions. These features result in the enhancement of the kinetics and the improvement of structural stability of the materials for lithium storage.

The morphologies of the EM−N−C−NiO NCs is significantly affected by the time of the heat treatment of the $Ni(HCO_3)_2$ precursors in $EMImBF_4$. When the precursors are treated in $EMImBF_4$ for 3−4 h at 180 °C and then calcined at 350 °C for 3 h under Ar atmosphere, we obtain the hollow-structured clusters, which are generated by the assembly of the NiO NCs (Figure S3B, C). When the heat treatment time in $EMImBF_4$ is less than 3 h (for example 2 h), we cannot obtain hollow-structured clusters. Instead, the solid clusters are produced as observed from TEM images (Figure S3A). However, long time treatment of the precursors in $EMImBF_4$ (for example 5 h) causes the complete breakage of the clusters (Figure S3D). Therefore, the heat treatment of the $Ni(HCO_3)_2$ in $EMImBF_4$ for 3−4 h can ensure the formation of the hollow-structured cluster under our experimental conditions. We also studied the effects of heat treatment temperature of $Ni(HCO_3)_2$ precursors in $EMImBF_4$ on the morphologies of the products. We obtain the hollow-structured assembly of the EM−N−C−NiO NCs when we change the heat treatment temperature in the range of 120−200 °C (Figure S4), implying the treated temperature has a negligible effect on the morphologies of the products in our experimental temperature range.

The compositions (refer to N/C atomic ratios) of the N-doped carbon layer on NiO NC s surface can be tuned by heat treatment of the $Ni(HCO_3)_2$ precursors in different ILs. We obtained the BM−N−C−NiO NCs and HM−N−C−NiO NCs by treating the precursors in $BMImBF_4$ and $HMImBF_4$, respectively. The presence of the N-doped carbon layer is verified by XPS (Figure 3A), Raman spectra (Figure 3B), and the observation from high-magnification TEM images (Figure S5A and S6A). Similar to the case of EM−N−C−NiO NCs, XRD patterns show that the prepared NiO NCs have cubic structures (Figure S7A), which are further verified by HRTEM images because the lattice spacing of 0.24 and 0.21 nm, corresponding to the interspaces of (111) and (200), respectively, planes of the cubic NiO, is clearly observed (Figure S5B and S6B). The NiO NCs also assemble to the hollow-structured clusters with a size of ∼250−300 nm (Figures S5C,D and S6C,D). The TGA measurements show

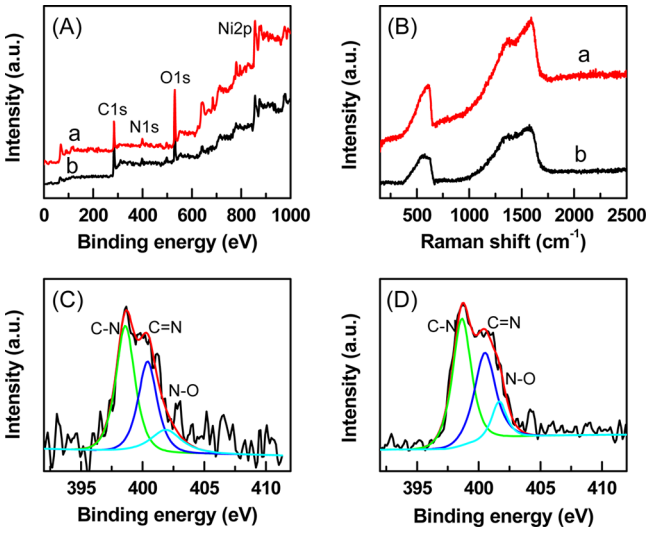

Figure 3. XPS survey spectra (A) and Raman spectra (B) of BM−N−C−NiO NCs (curve a) and HM−N−C−NiO NCs (curve b). (C and D) High-resolution XPS spectra of N 1s and their related curve-fitted components for BM−N−C−NiO NCs (C) and HM−N−C−NiO NCs (D). The black line is the measured data, and the red line is the curve-fitted data.

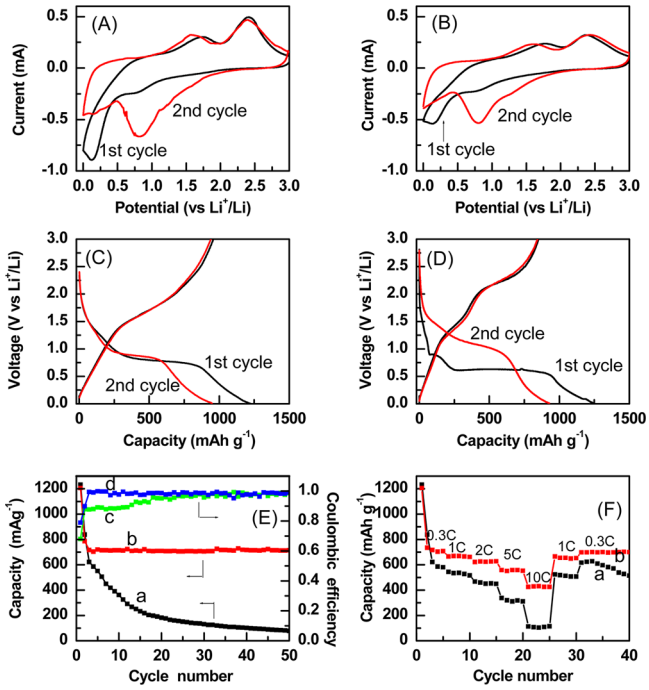

Figure 4. Typical CV responses of the EM−N−C−NiO NCs (A) and pristine NiO NPs (B) in a voltage range of 0−3 V (vs Li^+/Li) at a potential scan rate of 0.1 mV s^{-1}. (C and D) Voltage profiles of the first and second discharge−charge cycles for the EM−N−C−NiO NCs (C) and pristine NiO NPs (D) at a current rate of 0.3 C (~200 mA g^{-1}). (E) Capacity retention (a and b) and Coulombic efficiency (c and d) at a current rate of 0.3 C for the EM−N−C−NiO NCs (b and d) and pristine NiO NPs (a and c). (F) Rate capability of the EM−N−C−NiO NCs (b) and pristine NiO NPs (a) at different current rates (0.3−10 C).

the content of the N-doped carbon is ~13.4 and 11.6% (by weight) in BM−N−C−NiO NCs and HM−N−C−NiO NCs, respectively (Figure S7B).

XPS shows that the N/C atomic ratios in the N-doped carbon layer are ~12.5 and 8.4% for BM−N−C−NiO NCs and HM−N−C−NiO NCs, respectively. Deconvoluting the N peak shows that the surface nitrogen contains C−N, C═N, and N−O components in both the BM−N−C−NiO NCs and HM−N−C−NiO NCs, in good agreement with the EM−N−C−NiO NCs. The atomic compositions of C−N, C═N, and N−O components are ~46.5%, 44.4%, and 9.1%, respectively, for BM−N−C−NiO NCs (Figure 3C). These values change to ~50.4%, 38.5%, and 11.1% in HM−N−C−NiO NCs (Figure 3D). We also analyze the carbon functionalities and their distribution in the N-doped carbon layer, which shows the presence of C−C, C−O, C═O, O−C═O, C−N, and C═N components (Figure S8A,B). These results demonstrate that we can synthesize the N−C−NiO NCs with tunable N/C atomic ratios in the N-doped carbon coating by simply selecting different ILs.

3.2. Electrochemical Performances of the EM−N−C−NiO NCs. Having characterized the N−C−NiO NCs, we study the electrochemical performances of these prepared materials in LIBs in coin-type half cells (2025-type) at an ambient temperature. We first present the electrochemical performances of the EM−N−C−NiO NCs. For comparison, electrodes made of pristine NiO NPs were also measured under the same conditions. CV of the EM−N−C−NiO NCs exhibits two cathodic peaks (~0.77 and 0.12 V) and two anodic peaks (~1.73 and 2.41 V) in the first potential scanning cycle (Figure 4A). These peaks are typical indications of the initial reduction of NiO to Ni, and the electrochemical formation of Li_2O and a surface electrolyte interphase (SEI) layer, which results in irreversible capacity loss. The cathodic peak at ~0.77 V corresponds to the structure transition induced by lithium intercalation into crystalline NiO NCs ($NiO + xLi^+ + xe^- \rightarrow Li_xNiO$), and the peak at ~0.12 V is attributed to the reduction of Li_xNiO to Ni(0) with the formation of Li_2O ($Li_xNiO + (2-x)Li^+ + (2-x)e^- \rightarrow Li_2O + Ni$).[46] Two anodic peaks at ~1.73 and 2.41 V correspond to the partial decomposition of the SEI and Li_2O accompanying with the oxidation of metallic Ni, respectively, leading to the reformation of NiO. In the subsequent cycles, redox reactions of lithium ions insertion/extraction are highly reversible, where the cathodic lithium insertion occurs at ~0.82 V and the anodic lithium extraction occurs at ~2.41 V (Figure 4A). These characteristics are similar to those of the pristine NiO NPs (Figure 4B).

Lithium storage properties of EM−N−C−NiO NCs were evaluated by galvanostatic discharge−charge cycling. The first and second discharge−charge curves of the EM−N−C−NiO NCs and pristine NiO NPs at a current rate of 0.3 C (~200 mA g^{-1}) are presented in Figure 4, panels C and D, respectively. A voltage plateau appears at ~0.76 V during the first discharge process for the EM−N−C−NiO NCs (Figure 4C), which is in good agreement with the CV results. The initial discharge and charge capacities are ~1205 and 952 mAh g^{-1}, respectively. This values are much higher than the theoretical one (718 mAh g^{-1}), which is mainly attributed to the SEI film formation[56,57] and additional storage of Li^+ ions in the defects[58,59] (Figure 2B) or the pores of the hollow-structured clusters formed by assembly of NiO NCs (Figure 2E, F). Indeed, we can see the presence of crystal defects in NiO NCs from the HRTEM image in Figure 2B. Although the first discharge capacity of the EM−N−C−NiO NCs is slightly lower than that of pristine NiO NPs, which deliver specific capacities of ~1232 and 838 mAh g^{-1} in the first discharge and charge process, respectively (Figure 4D), its Coulombic efficiency (~79%) is higher than

dx.doi.org/10.1021/am500737w | ACS Appl. Mater. Interfaces 2014, 6, 7346−7355

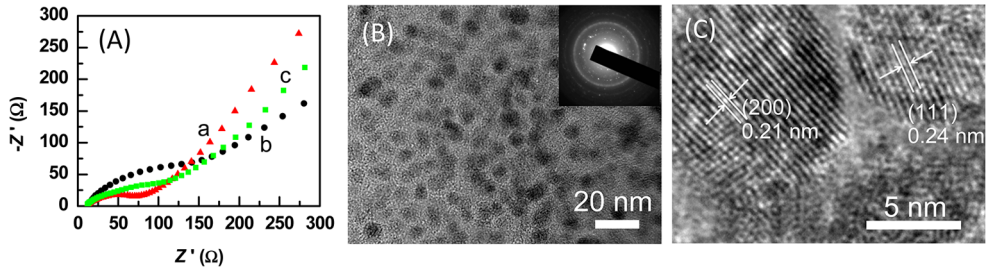

Figure 5. (A) Electrochemical impedance spectra of the electrode (EM−N−C−NiO NCs) at 0th (a), 5th (b), and 50th (c) discharge−charge cycle (at current rate of 0.3 C) in a coin half cell over the frequency range from 100 kHz to 0.01 Hz. (B and C) Low-magnification TEM (B) and HRTEM images (C) of the EM−N−C−NiO NCs after 50 discharge−charge cycles at a current rate of 0.3 C. The inset in (B) shows the SAED pattern of the NiO NCs.

that of pristine NiO NPs (∼68%), indicating that the discharge−charge kinetics of the EM−N−C−NiO NCs is improved by coating the N-doped carbon layer. The fast kinetics of the EM−N−C−NiO NCs are due to the small size of the NiO NCs and the unique hollow-structured cluster networks, which shortens the diffusion path for both electrons and Li^+ ions. Moreover, the intimate interaction between the highly conductive N-doped carbon layer and the NiO NCs makes the EM−N−C−NiO NCs electrochemically active because the charge carriers can be effectively and rapidly conducted back and forth between the NiO NCs and the current collector through the highly conducting N-doped carbon layer. The Coulombic efficiency of the EM−N−C−NiO NCs approaches 100% in the following cycle (Figure 4C), implying a facile lithium ions insertion−extraction associated with efficient transport of ions and electrons in the materials due to the higher surface electronic conductivity of the N-doped carbon layer.

The discharge−charge stability of the EM−N−C−NiO NCs was estimated and compared with that of pristine NiO NPs. The discharge capacity of the EM−N−C−NiO NCs is ∼784 mAh g^{-1} at the second discharge−charge cycle, and then saturates to ∼710 mAh g^{-1} (almost the same as the theoretical capacity of NiO (718 mAh g^{-1})) at the third discharge−charge cycle, and maintains at this reversible value at least up to the 50th cycle (curve b, Figure 4E). However, the discharge capacity of the pristine NiO NPs decreases significantly with the increasing of the discharge−charge cycles and is ∼80 mAh g^{-1} after 50 cycles (curve a, Figure 4E), which is ∼9 times lower than that of the EM−N−C−NiO NCs. The Coulombic efficiencies of the EM−N−C−NiO NCs are stable and remain ∼98−99% (curve d, Figure 4E), while the pristine NiO NPs shows obviously lower Coulombic efficiencies in the fifth−20th cycles (curve c, Figure 4E). The superior cycling performance of the EM−N−C−NiO NCs should be due to that the presence of N-doped carbon coating on the surface of NiO NCs because the N-doped carbon layer with higher conductivity can not only buffer the volume change but also prevent the aggregation of the active materials upon cycling. In contrast, the large volume change, poor electronic conductivity, and aggregation of NiO NPs during the charge−discharge cycles can lead to the inferior cycling performance of pristine NiO NPs.

The high-rate capability of the EM−N−C−NiO NCs was also studied to examine its feasibility for future battery applications, such as in electric vehicles that require high power density during operation. The discharge capacities were measured from current rate of 0.3 to 10 C for five cycles at each current rate. The discharge capacities of the pristine NiO NPs decrease rapidly with the increasing of the current rates (curve a, Figure 4F). Although the discharge capacities of the EM−N−C−NiO NCs also decease with the increasing of the discharge current rates (curve b, Figure 4F), their capacities are higher than those of the pristine NiO NPs at every discharge current rate. For example, the EM−N−C−NiO NCs is still able to deliver a discharge capacity of ∼430 mAh g^{-1} at a current density of 10 C, which is much higher than the pristine NiO NPs (∼100 mAh g^{-1}), indicative of good capacity retention of the EM−N−C−NiO NCs at a high current rate. Moreover, the reversible capacity of the EM−N−C−NiO NCs is retained upon cycling at all rates tested. A capacity of ∼695 mAh g^{-1} at a current rate of 0.3 C is retained after 50 discharge−charge cycles at various current rates (curve b, Figure 4F), indicating good cycling stability.

The high rate capacity and good cycling stability of the EM−N−C−NiO NCs are also due to the small size of the NiO NCs and the unique hollow-structured cluster networks, which shortens the diffusion path for both electrons and Li^+ ions, ensures a high electrode−electrolyte contact area, offers more active sites for electrochemical reactions, and effectively handles the volume change during discharge−charge processes. In addition, the highly conductive N-doped carbon layer makes the EM−N−C−NiO NCs electrochemically active because the charge carriers can be effectively and rapidly conducted back and forth between the NiO NCs and the current collector during the intercalation-extraction processes of lithium ions.

To understand the interfacial behavior of the EM−N−C−NiO NCs during the cycling processes, electrochemical impedance spectroscopy (EIS) was recorded at the different discharge−charge cycles (at the zeroth, fifth, and 50th cycle). The Nyquist plots for the electrode at the zeroth, fifth, and 50th cycle show similar intercepts (∼8 Ω, curves a−c, Figure 5A) with the real impedance axis (Z' axis). This resistance represents ohmic resistance from the contact, electrode, and electrolyte.[60] This value is about half of that for the pristine NiO NPs (∼17 Ω, Figure S9), indicative of the high surface electronic conductivity of the N-doped carbon layer. With frequency decreases, the Nyquist plot exhibits a semicircle corresponding to the charge transfer resistance of the electrochemical process. Before discharge−charge cycle (fresh electrode), the EM−N−C−NiO NCs electrode shows a smaller diameter of the semicircle (∼65 Ω, curve a, Figure 5A) than the pristine NiO NPs (∼160 Ω, Figure S9), suggesting that the EM−N−C−NiO NCs possess smaller charge transfer resistance and therefore a facile lithium ions insertion/extraction. The charge transfer resistance increases to

be ~170 Ω after 5 cycles (curve b, Figure 5A), which is caused by the formation of SEI.[20] The charge transfer resistance, however, decreases to be ~130 Ω after 50 discharge−charge cycles (curve c, Figure 5A), implying that the electron conduction and ion diffusion pathways in the material are not affected by forming SEI during cycling. This nature is supported by the fact that the electrode can still retain high capacities after 50 discharge−charge cycles (Figure 4E). This feature has been seldom achieved using traditional electrode structure for transition metal oxide anodes.

The slope in the low-frequency region after the semicircle reflects the diffusion resistance of the electrolyte ions into the electrode material.[61] After 5 discharge−charge cycles, the slope at the low-frequency region is decreased (curves a and b, Figure 5A), indicating an increased diffusion resistance, which is also caused by the formation of SEI layer. However, the slope shows a similar feature to the fresh electrode after 50 cycles (curve c, Figure 5A), suggesting that facile lithium diffusion channels can be produced during the reversible insertion/extraction processes.

After the 50 discharge−charge cycles, the morphology and structure of the EM−N−C−NiO NCs were examined by TEM and compared with that before cycling (Figure 5B,C). It reveals that the EM−N−C−NiO NCs almost retain their original morphologies, demonstrating the long-term stability of the prepared materials as anode in LIBs. The NiO NCs are embedded in the N-doped carbon layer (Figure 5B), which can provide space for buffering volume changes upon cycling. In particular, the aggregation of the NiO NCs is avoided under the protection of the N-doped carbon layer. HRTEM image shows the lattice spacing of 0.24 and 0.21 nm for interspaces of (111) and (200), respectively (Figure 5C), which are the same as those for NiO NCs before discharge−charge cycling (Figure 2B). The corresponding SAED pattern shows concentric rings composed of bright discrete diffraction spots (Figure 5D), indicating that the electrode material still remains the high degree of crystallinity after 50 discharge−charge cycles. These features suggest a highly reversible conversion reaction of the prepared material. For transition metal oxides as anode materials, large volume change and stresses accompanying the phase transition upon lithium ions intercalation-extraction usually cause pulverization of the electrode, which leads to weak contact of the materials and fast decay in capacity upon cycling. Our prepared EM−N−C−NiO NCs can effectively avoid the problems of cracking or pulverization and exhibit long-term stability and integrity upon cycling.

3.3. N/C-Atomic-Ratio-Dependent Performances of N−C−NiO NCs. We next studied the effects of N/C atomic ratios of the N-doped carbon layer on the electrochemical performances of the N−C−NiO NCs. We compared the discharge−charge stability (at 0.3 C) and the high current rate capacities of the EM−N−C−NiO NCs, BM−N−C−NiO NCs, and HM−N−C−NiO NCs. The N/C ratios in the N-doped carbon layer are ~21.2, 12.5, and 8.4% (by weight) for EM−N−C−NiO NCs, BM−N−C−NiO NCs, and HM−N−C−NiO NCs, respectively. The initial discharge capacity is almost independent of the compositions of the N-doped carbon coating, and is ~1210 mAh g^{-1} for the EM−N−C−NiO NCs, BM−N−C−NiO NCs, and HM−N−C−NiO NCs (Figure 6A. Note that, for better comparison, the potential profile of discharge process for the EM−N−C−NiO NCs is also depicted in Figure 6A; therefore, curve a in Figure 6A is the same as curve b in Figure 4E). The discharge capacities decrease rapidly

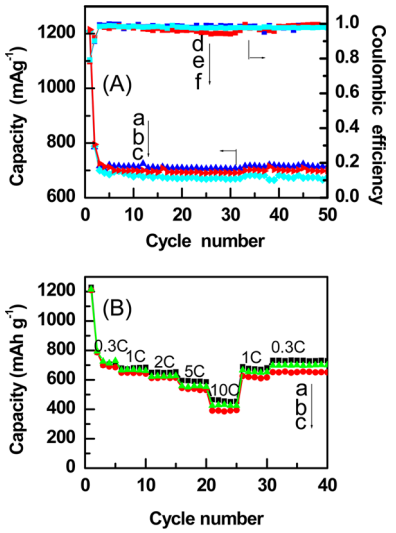

Figure 6. (A) Capacity retention (curves a−c) and Coulombic efficiency (curves c−e) at a current rate of 0.3 C for the EM−N−C−NiO NCs (curves a and d), BM−N−C−NiO NCs (curves b and e), and HM−N−C−NiO NCs (curves c and f). (B) Rate capability of the EM−N−C−NiO NCs (curve a), BM−N−C−NiO NCs (curve b), and HM−N−C−NiO NCs (curve c) at different current rates (0.3−10 C).

with the increasing of the discharge−charge cycles, and saturate to a stable value after 3 cycles. The reversible discharge capacity increases with the increasing of the N/C ratios in the carbon coating. They are ~710, 690, and 680 mAh g^{-1} for the EM−N−C−NiO NCs, BM−N−C−NiO NCs, and HM−N−C−NiO NCs, respectively (curves a−c, Figure 6A). However, the Coulombic efficiencies are almost independent of the N/C ratios in the N-doped carbon coating and are ~99% for the EM−N−C−NiO NCs, BM−N−C−NiO NCs, and HM−N−C−NiO NCs (curves d−f, Figure 6A). The high-rate capability was also measured from current rate of 0.3 to 10 C for five cycles at each current rate. The discharge capacities at each discharge current rate are slightly increased with the order of the EM−N−C−NiO NCs, BM−N−C−NiO NCs, and HM−N−C−NiO NCs (Figure 6B), implying that capacity retention of the N−C−NiO NCs at high current rate is enhanced with increasing of N/C ratios in the N-doped carbon layer. Moreover, the reversible capacity is retained upon cycling at all rates tested. A capacity of approximately 690, 670, and 650 mAh g^{-1} at a current rate of 0.3 C is retained for EM−N−C−NiO NCs, BM−N−C−NiO NCs, and HM−N−C−NiO NCs, respectively, after 50 discharge−charge cycles at various current rates (Figure 6B), indicating cycling stability is also enhanced with increasing of the N/C ratios in the N-doped carbon layer.

The high electrochemical performances of the N−C−NiO NCs at the high N/C atomic ratios in the N-doped carbon coating may be probably due to the enhancement of the electronic conductivity of the carbon coating after nitrogen doping. Our previous results (based on DFT calculations) indicated that the N atom is quite negative in the N-doped carbon layer (used graphene as a calculation model), resulting from the consequence of N atoms having a more electronegative and strong electron-accepting ability than carbon.[53,62] Most of the compensating positive charge is distributed on the adjacent carbon atoms; therefore, the charges of the carbon atoms adjacent to the doped N atom have significant enhancement in comparison with those in the case of pure

carbon. In contrast, the carbon atoms in the undoped carbon layer are almost neutral except that those carbon atoms at the edge of the carbon plane having a very weak negative charge. The doped nitrogen-induced charge enhancement of the carbon atoms adjacent to the N atom and charge delocalization could be favorable for the improvement of the electronic conductivity of the N-doped carbon layer. This improvement will be further enhanced with the increasing of the N level in the N-doped carbon layer. Moreover, our previous results indicated that the doped N atom can also alter the distribution of electrostatic potential (EP), which expresses the net electrical effect of the electrons and nuclei of a system on the surrounding space and is a useful property for analyzing and predicting a wide range of microscopic properties of chemical systems,[63] on carbon atoms. The EP distributes uniformly on the each carbon atom for the undoped carbon system. Nitrogen doping produces an obvious positive EP region for the carbon atoms around the doped nitrogen atom. The presence of the positive EP region can enhance the ability of N-doped carbon to donate electrons, which is helpful for the intercalation–extraction process of lithium ions.[47]

4. CONCLUSIONS

In conclusion, we have synthesized N-doped carbon-coated NiO nanocrystals (N–C–NiO NCs) with use of the nitrogen-containing ionic liquids (ILs) as new carbon precursor. The compositions (N/C ratios) in the N-doped carbon layer can be easily tuned by selecting different ILs. When evaluated as anode for LIBs, the synthesized EM–N–C–NiO NCs (with the N/C ratio of 21.2% in the N-doped carbon layer) show good electrochemical performance with a high specific capacity (~710 mAh g^{-1} at a current rate of 0.3 C), a high rate capability (still delivers a discharge capacity of ~430 mAh g^{-1} at a current density of 10 C), and good capacity retention upon cycling (the discharge capacity remains almost unchangeable after 50 discharge–charge cycles at 0.3 C). Moreover, the electrochemical performances of the N–C–NiO NCs are enhanced with increasing of the N/C ratios in the N-doped carbon layer. These improved electrochemical properties of the N–C–NiO NCs are primarily attributed to that the presence of N-doped carbon coating on the surface of NiO NCs, which can significantly enhance the electronic conductivity, effectively avoid the problems of cracking or pulverization of the NiO, and prevent the aggregation of the active materials upon cycling. All of these properties make this synthesized material a promising anode material for LIBs. Considering that NiO is cost-effective and easy production of ILs has been realized, such material holds great potential for real application. Our approach offers an effective and convenient technique to improve the specific capacities and rate capabilities of highly insulating electrode materials for batteries and may also provide general and effective approach toward the synthesis of other metal oxides coated with N-doped carbon layer.

■ ASSOCIATED CONTENT

Supporting Information

The detailed characterization (including XRD, TGA, XPS, SEM, and TEM) of $Ni(HCO_3)_2$ precursor, BM–N–C–NiO NCs, and HM–N–C–NiO NCs, the SEM and TEM images of the NiO NPs, dependence of the morphologies of the EM–N–C–NiO NCs on the heat treatment temperature of the $Ni(HCO_3)_2$ precursors in $EMImBF_4$, and EIS of the fresh pristine NiO NPs electrode. This material is available free of charge via the Internet at http://pubs.acs.org.

■ AUTHOR INFORMATION

Corresponding Authors

*E-mail: wuping_nj@126.com.
*E-mail: cxcai@njnu.edu.cn.

Notes

The authors declare no competing financial interest.

■ ACKNOWLEDGMENTS

This work is supported by NSFC (21175067, 21273117, 21375063, and 21335004), NSF of Jiangsu Province (BK2011779), China Postdoctoral Science Foundation (2013M541695), the Foundation of the Education Department of Jiangsu Province (13KJB150024), the Program for Outstanding Innovation Research Team of Universities in Jiangsu Province, and the Priority Academic Program Development of Jiangsu Higher Education Institutions.

■ REFERENCES

(1) Goodenough, J. B.; Park, K.-S. The Li-Ion Rechargeable Battery: A Perspective. *J. Am. Chem. Soc.* **2013**, *135*, 1167–1176.
(2) Jiang, J.; Li, Y.; Liu, J.; Huang, X.; Yuan, C.; Lou, X. W. Recent Advances in Metal Oxide-based Electrode Architecture Design for Electrochemical Energy Storage. *Adv. Mater.* **2012**, *24*, 5166–5180.
(3) Larcher, D.; Beattie, S.; Morcrette, M.; Edström, K.; Jumas, J.-C.; Tarascon, J.-M. Recent Findings and Prospects in the Field of Pure Metals as Negative Electrodes for Li-Ion Batteries. *J. Mater. Chem.* **2007**, *17*, 3759–3772.
(4) Zhu, G.-N.; Wang, Y.-G.; Xia, Y.-Y. Ti-Based Compounds as Anode Materials for Li-Ion Batteries. *Energy Environ. Sci.* **2012**, *5*, 6652–6667.
(5) Subban, C. V.; Ati, M.; Rousse, G.; Abakumov, A. M.; Tendeloo, G. V.; Janot, R.; Tarascon, J.-M. Preparation, Structure, and Electrochemistry of Layered Polyanionic Hydroxysulfates: $LiMSO_4OH$ (M = Fe, Co, Mn) Electrodes for Li-Ion Batteries. *J. Am. Chem. Soc.* **2013**, *135*, 3653–3661.
(6) Cho, Y. J.; Im, H. S.; Kim, H. S.; Myung, Y.; Back, S. H.; Lim, Y. R.; Jung, C. S.; Jang, D. M.; Park, J.; Cha, E. H.; Cho, W. I.; Shojaei, F.; Kang, H. S. Tetragonal Phase Germanium Nanocrystals in Lithium Ion Batteries. *ACS Nano* **2013**, *7*, 9075–9084.
(7) Yoon, S.; Liao, C.; Sun, X.-G.; Bridges, C. A.; Unocic, R. R.; Nanda, J.; Dai, S.; Paranthaman, M. P. Conductive Surface Modification of $LiFePO_4$ with Nitrogen-Doped Carbon Layers for Lithium-Ion Batteries. *J. Mater. Chem.* **2012**, *22*, 4611–4614.
(8) Zhou, W.; Chen, H.; Yu, Y.; Wang, D.; Cui, Z.; DiSalvo, F. J.; Abruña, H. D. Amylopectin Wrapped Graphene Oxide/Sulfur for Improved Cyclability of Lithium-Sulfur Battery. *ACS Nano* **2013**, *7*, 8801–8808.
(9) Becker, C. R.; Strawhecker, K. E.; McAllister, Q. P.; Lundgren, C. A. *In Situ* Atomic Force Microscopy of Lithiation and Delithiation of Silicon Nanostructures for Lithium Ion Batteries. *ACS Nano* **2013**, *7*, 9173–9182.
(10) Sun, C.; Rajasekhara, S.; Goodenough, J. B.; Zhou, F. Monodisperse Porous $LiFePO_4$ Microspheres for a High Power Li-Ion Battery Cathode. *J. Am. Chem. Soc.* **2011**, *133*, 2132–2135.
(11) Yin, Y.; Hu, Y.; Wu, P.; Zhang, H.; Cai, C. A Graphene-Amorphous $FePO_4$ Hollow Nanosphere Hybrid as a Cathode Material for Lithium Ion Batteries. *Chem. Commun.* **2012**, *48*, 2137–2139.
(12) Yin, Y.; Wu, P.; Zhang, H.; Cai, C. Enhanced Cathode Performances of Amorphous $FePO_4$ Hollow Nanospheres with Tunable Shell Thickness in Lithium Ion Batteries. *Electrochem. Commun.* **2012**, *18*, 1–3.

(13) Zhang, X.; Cheng, F.; Yang, J.; Chen, J. $LiNi_{0.5}Mn_{1.5}O_4$ Porous Nanorods as High-Rate and Long-Life Cathode for Li-Ion Batteries. *Nano Lett.* **2013**, *13*, 2822−2825.
(14) Ma, H.; Zhang, S.; Ji, W.; Tao, Z.; Chen, J. α-CuV_2O_6 Nanowires: Hydrothermal Synthesis and Primary Lithium Battery Application. *J. Am. Chem. Soc.* **2008**, *130*, 5361−5367.
(15) Chen, Y.; Li, X.; Park, K.; Song, J.; Hong, J.; Zhou, L.; Mai, Y.-W.; Huang, H.; Goodenough, J. B. Hollow Carbon-Nanotube/Carbon-Nanofiber Hybrid Anodes for Li-Ion Batteries. *J. Am. Chem. Soc.* **2013**, *135*, 16280−16283.
(16) Whittingham, M. S. Lithium Batteries and Cathode Materials. *Chem. Rev.* **2004**, *104*, 4271−4302.
(17) Wang, Y.-Q.; Gu, L.; Guo, Y.-G.; Li, H.; He, X.-Q.; Tsukimoto, S.; Ikuhara, Y.; Wan, L.-J. Rutile-TiO_2 Nanocoating for a High-Rate $Li_4Ti_5O_{12}$ Anode of a Lithium-Ion Battery. *J. Am. Chem. Soc.* **2012**, *134*, 7874−7879.
(18) Qu, J.; Yin, Y.-X.; Wang, Y.-Q.; Yan, Y.; Guo, Y.-G.; Song, W.-G. Layer Structured α-Fe_2O_3 Nanodisk/Reduced Graphene Oxide Composites as High-Performance Anode Materials for Lithium-Ion Batteries. *ACS Appl. Mater. Interfaces* **2013**, *5*, 3932−3936.
(19) Shi, W.; Rui, X.; Zhu, J.; Yan, Q. Design of Nanostructured Hybrid Materials Based on Carbon and Metal Oxides for Li Ion Batteries. *J. Phys. Chem. C* **2012**, *116*, 26685−26693.
(20) Jia, X.; Chen, Z.; Cui, X.; Peng, Y.; Wang, X.; Wang, G.; Wei, F.; Lu, Y. Building Robust Architectures of Carbon and Metal Oxide Nanocrystals toward High-Performance Anodes for Lithium-Ion Batteries. *ACS Nano* **2012**, *6*, 9911−9919.
(21) Myung, S.-T.; Kikuchi, M.; Yoon, C. S.; Yashiro, H.; Kim, S.-J.; Sun, Y.-K.; Scrosati, B. Black Anatase Titania Enabling Ultra High Cycling Rates for Rechargeable Lithium Batteries. *Energy Environ. Sci.* **2013**, *6*, 2609−2614.
(22) Liu, J.; Hou, M.; Guo, S.; Wang, C.; Xia, Y. Improving the Electrochemical Performances of Layered Lithium-Rich Transition-Metal Oxides by Controlling the Structural Defects. *Energy Environ. Sci.* **2014**, *7*, 705−714.
(23) Kravchyk, K.; Protesescu, L.; Bodnarchuk, M. I.; Krumeich, F.; Yarema, M.; Walter, M.; Guntlin, C.; Kovalenko, M. V. Monodisperse and Inorganically Capped Sn and Sn/SnO_2 Nanocrystals for High-Performance Li-Ion Battery Anodes. *J. Am. Chem. Soc.* **2013**, *135*, 4199−4202.
(24) Zhang, L.; Wu, H. B.; Madhavi, S.; Hng, H. H.; Lou, X. W. Formation of Fe_2O_3 Microboxes with Hierarchical Shell Structures from Metal-Organic Frameworks and Their Lithium Storage Properties. *J. Am. Chem. Soc.* **2012**, *134*, 17388−17391.
(25) Feckl, J. M.; Fominykh, K.; Döblinger, M.; Fattakhova-Rohlfing, D.; Bein, T. Nanoscale Porous Framework of Lithium Titanate for Ultrafast Lithium Insertion. *Angew. Chem., Int. Ed.* **2012**, *51*, 7459−7463.
(26) Li, W.; Wang, F.; Feng, S.; Wang, J.; Sun, Z.; Li, B.; Li, Y.; Yang, J.; Elzatahry, A. A.; Xia, Y.; Zhao, D. Sol-Gel Design Strategy for Ultradispersed TiO_2 Nanoparticles on Graphene for High-Performance Lithium Ion Batteries. *J. Am. Chem. Soc.* **2013**, *135*, 18300−18303.
(27) Ding, S.; Zhang, D.; Wu, H. B.; Zhang, Z.; Lou, X. W. Synthesis of Micro-Sized SnO_2@Carbon Hollow Spheres with Enhanced Lithium Storage Properties. *Nanoscale* **2012**, *4*, 3651−3654.
(28) Wang, Z.; Zhou, L.; Lou, X. W. Metal Oxide Hollow Nanostructured for Lithium-Ion Batteries. *Adv. Mater.* **2012**, *24*, 1903−1911.
(29) Wu, H. B.; Chen, J. C.; Hng, H. H.; Lou, X. W. Nanostructured Metal Oxide-Based Materials as Advanced Anodes for Lithium-Ion Batteries. *Nanoscale* **2012**, *4*, 2526−2542.
(30) Zhang, G.; Wu, H. B.; Hoster, H. E.; Lou, X. W. Strongly Coupled Carbon Nanofiber-Metal Oxide Coaxial Nanocables with Enhanced Lithium Storage Properties. *Energy Environ. Sci.* **2014**, *7*, 302−305.
(31) Wang, Z.; Wang, Z.; Liu, W.; Xiao, W.; Lou, X. W. Amorphous $CoSnO_3$@C Nanoboxes with Superior Lithium Storage Capability. *Energy Environ. Sci.* **2013**, *6*, 87−91.
(32) Su, Q.; Xie, D.; Zhang, J.; Du, G.; Xu, B. *In Situ* Transmission Electron Microscopy Observation of the Conversion Mechanism of Fe_2O_3/Graphene Anode during Lithiation-Delithiation Processes. *ACS Nano* **2013**, *7*, 9115−9121.
(33) Su, Q.; Chang, L.; Zhang, J.; Du, G.; Xu, B. *In Situ* TEM Observation of the Electrochemical Process of Individual CeO_2/Graphene Anode for Lithium Ion Battery. *J. Phys. Chem. C* **2013**, *117*, 4292−4298.
(34) Tian, B.; Światowska, J.; Maurice, V.; Zanna, S.; Seyeux, A.; Klein, L. H.; Marcus, P. Combined Surface and Electrochemical Study of the Lithiation/Delithiation Mechanism of the Iron Oxide Thin-Film Anode for Lithium-Ion Batteries. *J. Phys. Chem. C* **2013**, *117*, 21651−21661.
(35) Koo, B.; Xiong, H.; Slater, M. D.; Prakapenka, V. B.; Balasubramanian, M.; Podsiadlo, P.; Johnson, C. S.; Rajh, T.; Shevchenko, E. V. Hollow Iron Oxide Nanoparticles for Application in Lithium Ion Batteries. *Nano Lett.* **2012**, *12*, 2429−2435.
(36) Xie, D.; Su, Q.; Yuan, W.; Dong, Z.; Zhang, J.; Du, G. Synthesis of Porous NiO-Wrapped Graphene Nanosheets and Their Improved Lithium Storage Properties. *J. Phys. Chem. C* **2013**, *117*, 24121−24128.
(37) Paek, S.-M.; Yoo, E.; Honma, I. Enhanced Cyclic Performance and Lithium Storage Capacity of SnO_2/Graphene Nanoporous Electrodes with Three-Dimensionally Delaminated Flexible Structure. *Nano Lett.* **2009**, *9*, 72−75.
(38) Latorre-Sanchez, M.; Atienzar, P.; Abellán, G.; Puche, M.; Fornés, V.; Ribera, A.; García, H. The Synthesis of a Hybrid Graphene-Nickel/Manganese Mixed Oxide and Its Performance in Lithium-Ion Batteries. *Carbon* **2012**, *50*, 518−525.
(39) Li, J.; Zhao, Y.; Wang, N.; Ding, Y.; Guan, L. Enhanced Performance of a MnO_2-Graphene Sheet Cathode for Lithium Ion Batteries Using Sodium Alginate as A Binder. *J. Mater. Chem.* **2012**, *22*, 13002−13004.
(40) Zhao, J.; Tao, Z.; Liang, J.; Chen, J. Facile Synthesis of Nanoporous γ-MnO_2 Structures and Their Application in Rechargeable Li-Ion Batteries. *Cryst. Growth Des.* **2008**, *8*, 2799−2805.
(41) Cheng, F.; Zhao, J.; Song, W.; Li, C.; Ma, H.; Chen, J.; Shen, P. Facile Controlled Synthesis of MnO_2 Nanostructures of Novel Shapes and Their Application in Batteries. *Inorg. Chem.* **2006**, *45*, 2038−2044.
(42) Wang, G. J.; Gao, J.; Fu, L. J.; Zhao, N. H.; Wu, Y. P.; Takamura, T. Preparation and Characteristic of Carbon-Coated $Li_4Ti_5O_{12}$ Anode Material. *J. Power Sources* **2007**, *174*, 1109−1112.
(43) Wang, Y.; Wang, Y.; Hosono, E.; Wang, K.; Zhou, H. The Design of a $LiFePO_4$/Carbon Nanocomposite with a Core-Shell Structure and Its Synthesis by an In Situ Polymerization Restriction Method. *Angew. Chem., Int. Ed.* **2008**, *47*, 7461−7465.
(44) Wang, Y.; Liu, H.; Wang, K.; Eiji, H.; Wang, Y.; Zhou, H. Synthesis and Electrochemical Performance of Nano-Sized $Li_4Ti_5O_{12}$ with Double Surface Modification of Ti(III) and Carbon. *J. Mater. Chem.* **2009**, *19*, 6789−6795.
(45) Yan, X.; Tong, X.; Wang, J.; Gong, C.; Zhang, M.; Liang, L. Hydrothermal-Synthesized NiO Nanowall Array for Lithium Ion Batteries. *J. Alloys Compd.* **2013**, *556*, 56−61.
(46) Paraknowitsch, J. P.; Zhang, J.; Su, D.; Thomas, A.; Antonietti, M. Ionic Liquids as Precursors for Nitrogen-Doped Graphitic Carbon. *Adv. Mater.* **2010**, *22*, 87−92.
(47) Ding, Z.; Zhao, L.; Suo, L.; Jiao, Y.; Meng, S.; Hu, Y.-S.; Wang, Z.; Chen, L. Towards Understanding the Effects of Carbon and Nitrogen-Doped Carbon Coating on the Electrochemical Performance of $Li_4Ti_5O_{12}$ in Lithium Ion Batteries: A Combined Experimental and Theoretical Study. *Phys. Chem. Chem. Phys.* **2011**, *13*, 15127−15133.
(48) Zhao, L.; Hu, Y.-S.; Li, H.; Wang, Z.; Chen, L. Porous $Li_4Ti_5O_{12}$ Coated with N-doped Carbon from Ionic Liquids for Li-Ion Batteries. *Adv. Mater.* **2011**, *23*, 1385−1388.
(49) Yang, W.; Fellinger, T.-P.; Antonietti, M. Efficient Metal-Free Oxygen Reduction in Alkaline Medium on High-Surface-Area Mesoporous Nitrogen-Doped Carbons Made from Ionic Liquids and Nucleobases. *J. Am. Chem. Soc.* **2011**, *133*, 206−209.

(50) Lee, J. S.; Wang, X.; Luo, H.; Baker, G. A.; Dai, S. Facile Ionothermal Synthesis of Microporous and Mesoporous Carbons from Task Specific Ionic Liquids. *J. Am. Chem. Soc.* **2009**, *131*, 4596−4597.
(51) Zhu, G.; Xi, C.; Xu, H.; Zheng, D.; Liu, Y.; Xu, X.; Shen, X. Hierarchical NiO Hollow Microspheres Assembled from Nanosheet-Stacked Nanoparticles and Their Application in A Gas Sensor. *RSC Adv.* **2012**, *2*, 4236−4241.
(52) Wu, P.; Cai, Z.; Gao, Y.; Zhang, H.; Cai, C. Enhancing the Electrochemical Reduction of Hydrogen Peroxide Based on Nitrogen-Doped Graphene for Measurement of Its Releasing Process from Living Cells. *Chem. Commun.* **2011**, *47*, 11327−11329.
(53) Wu, P.; Qian, Y.; Du, P.; Zhang, H.; Cai, C. Facile Synthesis of Nitrogen-Doped Graphene for Measuring the Releasing Process of Hydrogen Peroxide from Living Cells. *J. Mater. Chem.* **2012**, *22*, 6402−6412.
(54) Yang, S.; Feng, X.; Wang, X.; Müllen, K. Graphene-Based Carbon Nitride Nanosheets as Efficient Metal-Free Electrocatalysts for Oxygen Reduction Reactions. *Angew. Chem., Int. Ed.* **2011**, *50*, 5339−5343.
(55) Kim, M.; Hwang, S.; Yu, J.-S. Novel Ordered Nanoporous Graphitic Carbon Nitride with C_3N_4 Stoichiometry as a Support for Pt-Ru Anode Catalytic in DMFC. *J. Mater. Chem.* **2007**, *17*, 1656−1659.
(56) Gnanaraj, J. S.; Zinigrad, E.; Asraf, L.; Sprecher, M.; Gottlieb, H. E.; Geissler, W.; Schmidt, M.; Aurbach, D. On the Use of $LiPF_3(CF_2CF_3)_3$ (LiFAP) Solutions for Li-Ion Batteries. Electrochemical and Thermal Studies. *Electrochem. Commun.* **2003**, *5*, 946−951.
(57) Aravindan, V.; Gnanaraj, J.; Madhavi, S.; Liu, H.-K. Lithium-Ion Conducting Electrolyte Salts for Lithium Batteries. *Chem.—Eur. J.* **2011**, *17*, 14326−14346.
(58) Kottegoda, I. R. M.; Idris, N. H.; Lu, L.; Wang, J.-Z.; Liu, H.-K. Synthesis and Characterization of Graphene-Nickel Oxide Nanostructures for Fast Charge-Discharge Application. *Electrochim. Acta* **2011**, *56*, 5815−5822.
(59) Tao, L.; Zai, J.; Wang, K.; Wan, Y.; Zhang, H.; Yu, C.; Xiao, Y.; Qian, X. 3D-Hierarchical NiO−Graphene Nanosheet Composites as Anodes for Lithium Ion Batteries with Improved Reversible Capacity and Cycle Stability. *RSC Adv.* **2012**, *2*, 3410−3415.
(60) Kou, Y.; Xu, Y.; Guo, Z.; Jiang, D. Supercapacitive Energy Storage and Electric Power Supply Using an Aza-Fused π-Conjugated Microporous Framework. *Angew. Chem., Int. Ed.* **2011**, *50*, 8753−8757.
(61) Largeot, C.; Portet, C.; Chmiola, J.; Taberna, P.-L.; Gogotsi, Y.; Simon, P. Relation between the Ion Size and Pore Size for an Electric Double-Layer Capacitor. *J. Am. Chem. Soc.* **2008**, *130*, 2730−2731.
(62) Wu, P.; Du, P.; Zhang, H.; Cai, C. Microscopic Effects of the Bonding Configuration of Nitrogen-Doped Graphene on Its Reactivity Toward Hydrogen Peroxide Reduction Reaction. *Phys. Chem. Chem. Phys.* **2013**, *15*, 6920−6928.
(63) Koleva, G.; Galabov, B.; Wu, J. I.; Schaefer, H. F.; Schleyer, P.; von, R. Electrophile Affinity: A Reactivity Measure for Aromatic Substitution. *J. Am. Chem. Soc.* **2009**, *131*, 14722−14727.